

# Fe-doped ceria solids synthesized by the microemulsion method for CO oxidation reactions

O.H. Laguna<sup>1\*</sup>, M.A. Centeno<sup>1</sup>, M. Boutonnet<sup>2</sup>, J.A. Odriozola<sup>1</sup>

<sup>1</sup>Departamento de Química Inorgánica e Instituto de Ciencia de Materiales de Sevilla, Centro Mixto Universidad de Sevilla-CSIC, Avenida Américo Vespucio 49, 41092 Seville, Spain

<sup>2</sup> Royal Institute of Technology (KTH), Department of Chemical Engineering and Technology, Div. of Chemical Technology, Teknikringen 42, S-10044 Stockholm, Sweden

\*Corresponding author: [oscarh@icmse.csic.es](mailto:oscarh@icmse.csic.es)

Tel: +34 954489221 / FAX: +34 954460665

## Abstract

A series of Ce-Fe mixed oxides as well as the pure oxides were synthesized by the microemulsions method. The solid solution formation was established for all the Fe-doped systems and only a hardly noticeable segregation of  $\alpha$ -Fe<sub>2</sub>O<sub>3</sub> was appreciated for the solid with the maximum iron content (50 Fe atomic%). The oxygen exchange is improved for all the Fe-doped systems; however the 10 Fe atomic% appears as the optimal iron content for achieving the maximum oxygen vacancies concentration and the higher reducibility efficiency. The CO oxidation (TOX, PROX) is especially achieved for the solids with the lower iron contents but with a superior oxygen vacancies proportion. These Ce-Fe systems prepared from microemulsions are very attractive to be considered as supports for depositing active phases capable of enhancing oxygen exchange ability of the whole system, allowing higher CO oxidation abilities.

## Keywords:

Water-in-oil microemulsion  
CO oxidation

Fe-doped ceria  
Oxygen vacancies

## 1. Introduction

CO oxidation processes are relevant from technological and environmental points of view. In this sense, the total (TOX) [1, 2] and the preferential oxidation of CO in presence of H<sub>2</sub> (PROX) have been widely studied. CO is a hazardous gas which is a concern in environmental protection. Its abatement from automobile exhaust gases and indoor air is an item of great importance. On the other hand, the PROX reaction generates a remarkable interest because it represents a key step in the H<sub>2</sub> fuel clean-up processes. The H<sub>2</sub> produced by reforming of organic molecules such as alcohols contains important amounts of H<sub>2</sub>O, CO<sub>2</sub> and CO. If this hydrogen is employed for fueling PEM fuel cells, ultralow levels of CO (commonly below 10 ppm) are mandatory in order to prevent the poisoning of the Pt-based PEMFC's catalysts [3]. The water gas shift reaction (WGS) is considered as the first cleaning step but it is unable to reduce the CO contents until the required levels and only 0.5-1% CO is achieved. So, an additional

CO abatement process is necessary and PROX reaction has demonstrated to be an efficient one.

Many systems have been studied as catalysts for the CO oxidation and it is generally accepted that reducible oxides such as  $\alpha$ -Fe<sub>2</sub>O<sub>3</sub>, TiO<sub>2</sub> and CeO<sub>2</sub> are attractive supports due to their capability to provide active oxygen species [4]. In the case of CeO<sub>2</sub>, it has been widely demonstrated that its oxygen mobility abilities can be improved by the modification of its structure through the doping with different cations such as Zr [5], Zn [6], Eu [7], Cu [8], and Fe [9] among others. This enhancement of the oxygen mobility is directly related to the formation of oxygen vacancies, which has been reported as maximum for contents of doping agent around 10 atomic% in Ce-Eu [7], Ce-Fe [10, 11] and Ce-Zn [6] systems. The promotion of oxygen vacancies in the modified ceria structures is especially attractive if these materials are employed as catalytic supports. For instance, in gold catalysts, besides the enhancement in oxygen mobility and redox properties of the solid, oxygen vacancies act as nucleation centers for gold deposition, favoring the gold dispersion and improving the catalytic performances towards CO oxidation [6, 10, 12, 13].

Fe-modified ceria systems present a remarkable improvement of their oxygen exchange abilities compared with the bare CeO<sub>2</sub>, because of the Ce-Fe synergy that is achieved by combining the redox behavior of the cerium (Ce<sup>4+</sup>/Ce<sup>3+</sup>) and iron (Fe<sup>3+</sup>/Fe<sup>2+</sup>) cations. Pérez-Alonso and coworkers have presented a complete study about the Ce-Fe interactions in several series of Ce-Fe mixed oxides prepared by coprecipitation [9, 14-16]. The catalytic performances of these materials were evaluated in the N<sub>2</sub>O decomposition and the Fisher-Tropsch synthesis. From these studies it can be pointed out that hematite-like and cubic ceria-like solid solutions are formed in the Ce-Fe systems, showing better catalytic performances than those of the pure oxides.

In a similar way, Bao et al reported the synthesis of Fe<sub>2</sub>O<sub>3</sub>-CeO<sub>2</sub> composites with different iron contents by coprecipitation, using urea as precipitation agent [11]. They found that there is a limit for the solid solution formation around 30 Fe molar percentages. The Ce<sub>0.9</sub>Fe<sub>0.1</sub> composite presented the best catalytic activity in the CO oxidation, which agrees with its highest amount of oxygen vacancies. However, we have recently presented the synthesis of Ce-Fe mixed oxides by thermal decomposition of the metallic propionates and although the solid with 10 Fe atomic% presented the solid solution formation and the highest CO oxidation performances, the Raman oxygen vacancies band was not detected [10].

From all above, it can be inferred that the synthesis procedure is determinant for the formation of the solid solution in Ce-Fe mixed systems and influences the mechanism of replacement of the Ce species by Fe ones into the ceria framework. In this sense, a synthesis method that ensures the homogeneity of the obtained mixed oxides is required and, the microemulsion method could be a promising one.

Microemulsion has been reported as a successful synthesis media for catalysts preparation offering particles in the nano-size range, high specific surface area and high metallic dispersion [17, 18]. Since the first report on the use of microemulsions in the preparation of noble-metal catalysts, different catalytic systems have been obtained successfully by this method, including oxide-based materials [19]. The synthesis of inorganic nanoparticles is commonly carried out in water-in-oil, which is one of the

three types of microemulsions [17]. This kind of microemulsion consists of small micelles at the microscopic level, being the water core of these micelles surrounded by surfactant molecules that allows stabilizing the dispersion of the aqueous phase in the oil phase. The precursor metallic salts are dissolved in the water cores and then precipitated by the adequate precipitating agent. This precipitating agent can be directly added to the microemulsion containing the metallic salts or also previously dissolved in a similar microemulsion which is later mixed with it. The type of oil phase, the composition of the water-in-oil microemulsion, the amount and type of surfactant and the type of precipitating agent are variables that have to be optimized for every system (to be prepared), in order to ensure the thermodynamic stability and the transparency (optical isotropy) of the microemulsion, because these features guarantee the strict control of the desired properties in the obtained material [17].

Considering the scenario presented above, in this paper the synthesis of a series of Fe-doped ceria samples employing microemulsions is explored. The microemulsion method was selected with the aim of preparing homogeneous Fe-doped ceria materials with improved Ce-Fe interactions and high potential applications as active support for CO oxidation reactions. For comparative purposes, pure oxides were prepared by the same procedure. All solids were characterized by means of XRF, BET, XRD, TPR-H<sub>2</sub>, UV-Vis and Raman spectroscopy. Finally, the catalytic performances of the obtained materials were evaluated in the TOX and PROX reactions and the results correlated with the observed structural modifications of the solids.

## 2. Experimental

### 2.1. Materials and methods

A series of Ce-Fe mixed oxides with different Fe content was prepared from microemulsion. N-octane was used as continuous oil phase, cetyl trimethyl ammonium bromide (CTAB) as the surfactant, 1-butanol as the cosurfactant and a solution of the metallic precursors as the aqueous phase. Ammonia (NH<sub>3</sub>) was used as precipitant. The composition of the microemulsion systems expressed as weight percentage (wt.%) is: 13% CTAB, 53% n-octane, 13% 1-butanol and 21% of aqueous phase (2M). The amounts of surfactant, cosurfactant and oil phase are similar to those reported by Palla et al. [20] and Nassos et al. [21].

The amounts of Fe and Ce in every solid were calculated as atomic percentages (atomic%) considering the moles of both cations. The Fe atomic% calculation is presented in equation 1. The intended values of Fe atomic% were 5, 10, 25 and 50%. Additionally pure cerium and iron oxides were synthesized for comparative purposes. The nomenclature for the prepared solids is CeO<sub>2</sub> and Fe<sub>2</sub>O<sub>3</sub> in the case of the pure oxides and CeFeX for the mixed oxides, being X the Fe atomic% (5, 10, 25 and 50).

$$Fe \text{ atomic\%} = \frac{molFe \times 100}{molFe + molCe} \quad \text{Eq. 1}$$

Previously, supplementary analysis were carried out with the aim of maximizing the concentration of the starting salts [Ce(NO<sub>3</sub>)<sub>3</sub> and Fe(NO<sub>3</sub>)<sub>2</sub>] in the aqueous phase while maintaining the optical isotropy [17]. For every Ce/Fe atomic ratio, the following molarities (M) were tested: 0.4; 1.0; 1.5 and 2M, where M is calculated according to

equation 2 and L is the volume of solution. The results of the isotropic stability study of the microemulsions (not shown) demonstrated that the maximum evaluated concentration (2M) can be employed [21-23].

$$M = \frac{[molCe + molFe]}{L} \quad \text{Eq. 2}$$

An excess of NH<sub>3</sub> (9:1 NH<sub>3</sub>/(Ce+Fe) molar ratio) was used as precipitating agent.

The synthesis was carried out as follows: Two microemulsion systems with the composition given in Table 1 were prepared separately. The first one, ME1, contains the adequate amounts of the metal nitrates in the aqueous solution, and the second one, ME2, contains the adequate amount of the precipitating agent (NH<sub>3</sub>) in the aqueous solution. Then, ME1 was added dropwise to the ME2 and precipitated particles were obtained. The mixture was kept under vigorous stirring during 24 hours at room temperature and after that, the particles were collected by centrifugation. The surfactant, cosurfactant and oil phase excesses were washed first with a 50/50 methanol/chloroform mixture and then with methanol. The obtained solid was dried at 60 °C during 24 h and finally calcined (10 °C/min) at 500 °C for 2 hours.

## 2.2. Characterization

The elemental composition of the samples was determined by X-ray fluorescence (XRF) spectrometry in a Panalytical AXIOS PW4400 sequential spectrophotometer with Rh tube as source of radiation. The measurements were performed onto pressed pellets containing 6 wt% wax.

The textural properties were studied by N<sub>2</sub> adsorption/desorption measurements at liquid nitrogen temperature in a Micromeritics ASAP 2010 apparatus. Before analysis, the samples were degassed at 150 °C for 2 hours under vacuum.

Powder X-ray diffraction (XRD) patterns were recorded on a Siemens D500 diffractometer, using Cu K $\alpha$  radiation (40 mA, 40 kV), with 0,017° step size and 275 s of step time, over a 2 $\theta$  range from 10 to 90°.

Raman spectra were recorded in a dispersive Horiva Jobin Yvon LabRam HR800 Confocal Raman Microscope with a green laser (532.14 nm) working at 5 mV power and using a 600 grooves/mm grating. The microscope used a 50x objective with a confocal pinhole of 1000  $\mu$ m.

The UV-Vis spectra were measured on a Varian<sup>®</sup> spectrometer model Cary 100, equipped with an integrating sphere and using BaSO<sub>4</sub> as reference. All the spectra were recorded in diffuse reflectance mode and transformed to a magnitude proportional to the extinction coefficient through the Kubelka-Munk function,  $F(\alpha)$ .

Temperature Programmed Reduction (TPR) experiments were carried out in a conventional quartz reactor connected to a TCD. The reactive gas stream (5% H<sub>2</sub> in Ar) was flowed at 50 mL/min over 50 mg of sample and the temperature raised at 10 °C/min from room temperature to 900 °C. A molecular sieve 13X was used to retain the

reduction products, mostly H<sub>2</sub>O and CO<sub>2</sub>. Quantitative analysis was done by integration of the reduction signal and comparison with hydrogen consumption of a CuO reference.

Catalytic activity: For the oxidation of CO (TOX), the solids (80 mg with 100 μm <math>\phi</math><math><200\ \mu\text{m}</math> particle size) were pretreated for 1 h at 300 °C in a 30 mL/min activation flow of 21vol% O<sub>2</sub> balanced in He. The light-off curves (from room temperature to 400 °C, 5°C/min) were obtained passing a 42 mL/min feed-stream of 3.4 vol% CO and 21 vol% O<sub>2</sub> balanced in He. The reaction was carried out in a conventional continuous flow U-shaped quartz reactor working at atmospheric pressure placing the sample between glass wools. The reaction products were followed by mass spectrometry (Balzers<sup>®</sup> Thermostar).

The preferential oxidation of CO in presence of hydrogen (PROX) was carried out at atmospheric pressure on a cylindrical stainless steel reactor (9 mm inner diameter), with 100 mL/min of a reaction mixture containing 2% CO, 1% O<sub>2</sub>, 50% H<sub>2</sub> and N<sub>2</sub> as balance. In order to avoid intrareactor gradients, the catalyst powder (100 mg, particle size  $\phi = 100\text{-}200\ \mu\text{m}$ ) was diluted with crushed inert glass with the same particle size until a reactor bed height of 5 mm. Before reaction, samples were activated for 1 h at 300 °C with a 21 vol% O<sub>2</sub> in N<sub>2</sub> flow (30 mL/min). Products and reactants were separated by on-line gas chromatography (Varian<sup>®</sup> CP-4900), equipped with a Poropak<sup>®</sup> Q, a Molecular Sieve 5A, and a TCD detector.

The CO conversion and the selectivity to CO oxidation were calculated according to equations 3 and 4 where CO<sub>in</sub> and O<sub>2in</sub> are the amounts of the CO and O<sub>2</sub> in the inlet and CO<sub>out</sub> and O<sub>2out</sub> are those of the outlet.

$$\text{CO conversion (\%)} = \frac{(CO_{in} - CO_{out}) \times 100}{CO_{in}} \quad (\text{Eq. 3})$$

$$\text{Selectivity to CO conversion (\%)} = \frac{(CO_{in} - CO_{out}) \times 100}{2(O_{2in} - O_{2out})} \quad (\text{Eq. 4})$$

### 3. Results and discussion

#### 3.1. XRF and textural analysis

The chemical composition of the prepared solids and the main textural properties are presented in Table 1.

The Ce and Fe atomic percentages are very close to the target values in all cases. This evidences that the microemulsion method allows a good control of the chemical composition of the prepared solids, as reported by Boutonnet et al. [17].

N<sub>2</sub> adsorption-desorption isotherms of the studied solids (not shown) present type II isotherms according to the IUPAC classification [24]. Type II isotherms are typical of macroporous systems where the monolayer formation at low relative pressure takes place. Then, as the relative pressure increases, the progressive multilayer adsorption is achieved [24]. In our case, since all solids present a small crystallite size (Table 1), that macroporosity is not due to the presence of macropores on the materials surface, but to

the N<sub>2</sub> condensation on the inter-nanoparticles spaces. The control of the crystallite size growing up for the obtained materials is one of the allowed features by the applied synthesis method. Microemulsion methodology inhibits the sintering of the nanoparticles because the initial interaction between both metals (Ce and Fe) is carried out into the aqueous phase of the micellar nanoreactors, generating very small nuclei where the formation of the mixed oxide is achieved, during the calcination.

In general, the BET surface areas and the pore volume values (Table 1) of the Fe-modified solids are higher than those of the pure oxides and increase with the iron content. However, the CeFe5 solid seems to present an additional promoting effect on the BET surface area considering the amount of iron incorporated.

### 3.2. XRD

The XRD patterns of the synthesized materials are presented in Figure 1.

The XRD profile of pure CeO<sub>2</sub> corresponds to c-CeO<sub>2</sub> fluorite structure (JCPDS 00-034-0394) and that of pure iron oxide correlates with the  $\alpha$ -Fe<sub>2</sub>O<sub>3</sub> phase (hematite). The mixed solids maintain the F-type crystalline structure characteristics of bare CeO<sub>2</sub>, although, for the solid with the highest amount of iron (CeFe50), a small reflection around 35° that could be attributed to the (110) plane of  $\alpha$ -Fe<sub>2</sub>O<sub>3</sub> is detected (see Figure 1B).

Besides, the diffraction lines of the doped-ceria systems shift towards higher angles as the amount of Fe increases, which is illustrated in the Figures 1A and 1B. This behavior is due to the contraction of the ceria network by the introduction of Fe<sup>3+</sup> ions at the Ce<sup>4+</sup> sites [10-12], since Fe<sup>3+</sup> cations are smaller than Ce<sup>4+</sup> ones. Consequently, a decrease in the measured ceria cell parameter is observed (Figure 2).

This decrease is linear until iron contents of 10 atomic%, which agrees with the Vegard's law which establishes that at a constant temperature, the cell parameters of an alloy should change linearly with the concentrations of its constituent elements [7, 25]. On the other hand, although the CeFe25 and CeFe50 solids also present a lower cell parameter respect to that of the bare CeO<sub>2</sub>, these values are out of the initial linear trend suggesting that the iron solubility becomes more difficult as the amount of iron increases. However, as the presence of segregated iron oxides are hardly noticeable even for the highest iron content introduced, we can conclude that most of the Fe species are forming part of the solid solution with ceria. Finally, the very small crystalline domain of the segregated iron oxides which difficulty their XRD detection, cannot be fully discarded.

The limited solubility of the Ce-Fe system has been established before [26]. We have shown in a previous work that the segregation of  $\alpha$ -Fe<sub>2</sub>O<sub>3</sub> was detected for iron contents higher than 10 atomic% in a series of Ce-Fe mixed oxides synthesized by a pseudo sol-gel method through the decomposition of the cerium and iron propionates [10]. In the same sense, Li et al. [27] also reported the 10 atomic% Fe as the maximum iron content able to form the Ce-Fe solid solution without segregation of iron oxides, in a series of mixed oxides prepared by co-precipitation with ammonia at pH around 8-10 [27]. Pérez-Alonso et al. [14] also studied the Ce-Fe mixed system synthesized by co-

precipitation with  $\text{NH}_4\text{OH}$ . They showed the formation of the solid solution without segregation of iron oxides for a Ce/Fe molar ratio as high as 1:1, when the solid is calcined at 300 °C. However they demonstrated the presence of  $\alpha\text{-Fe}_2\text{O}_3$  when the material was calcined at 500 °C. Later, Bao et al. [11] found a 30 Fe atomic% as the maximum iron content without segregation of the pure oxides in a series of Ce-Fe mixed oxides prepared by co-precipitation with urea. In spite of the high calcination temperature used in their work, (650 °C), they proposed that the preparation method is crucial in order to achieve the solid solution formation. They suggested that the Ce-Fe solid solution with a cubic structure is thermodynamically metastable and, at high temperatures, tends to the segregation of the pure oxides, which present a thermodynamically more stable configuration.

In the series of samples prepared in the present paper by microemulsion and calcined at 500°C, segregated iron oxides are only detected by XRD in an almost imperceptible way for the Fe content of 54.4 Fe atomic% contents (Figures 2 and 3). So, and taking into account the literature data cited above, the microemulsions methodology seems to favor a more stable and homogenous contact between Ce and Fe than other more conventional preparation methods, allowing to produce Ce-Fe solid solutions with higher iron contents [10, 11, 14, 27].

On the other hand, the crystallite size values of the pure oxides are higher than those of the mixed systems, Table 1. For the Ce-Fe solids, higher the iron content, lower the crystallite size. This behavior agrees with the reported inhibition of the sintering of ceria when introducing a doping cation inside its cubic structure, which provokes a decreasing in the ceria crystallite size with the amount of doping agent introduced [10, 13, 28, 29].

### 3.3. *Raman spectroscopy*

The Raman spectra of the prepared solids are presented in Figure 3. Bare  $\text{CeO}_2$  presents a peak at 458  $\text{cm}^{-1}$  that is ascribed to the Raman active  $\text{F}_{2g}$  mode, due to the oxygen symmetric breathing vibration around  $\text{Ce}^{4+}$  [7, 10, 30]. Besides this, a small band at ca. 598  $\text{cm}^{-1}$  ascribed to the presence of oxygen vacancies (Ov) [7, 12, 30] is detected.

The spectrum of pure  $\text{Fe}_2\text{O}_3$  shows bands attributed to the  $\alpha\text{-Fe}_2\text{O}_3$  structure (hematite) with the  $D_{3d}^6$  crystal space group (Figure 3 inset), confirming the XRD results previously discussed. The hematite, which is basically an antiferromagnetic material with a corundum-type structure, presents a high symmetry allowing seven active Raman phonons which appear below 620  $\text{cm}^{-1}$  [31-35]. The symmetry associated to every peak is presented in Figure 3 inset, pointing out that the band at 286  $\text{cm}^{-1}$  ( $\text{E}_g + \text{E}_g$ ) represents a doublet of  $\text{E}_g$  symmetry [31-35].

The Raman spectra of the mixed oxides are dominated by the  $\text{F}_{2g}$  signal of the  $\text{CeO}_2$  structure. For the solids with 5 and 10 Fe atomic % contents, this signal does not suffer a clear shift but it becomes broad. However, at higher iron contents, this signal broads and shifts to lower frequencies compared with that of the pure  $\text{CeO}_2$ . In addition for these solids, a shoulder around 370  $\text{cm}^{-1}$  becomes visible.

The detected modifications in the shape of the  $\text{F}_{2g}$  signal evidence the Fe-Ce interaction in the doped systems [12]. The introduction of  $\text{Fe}^{3+}$  cations into the ceria lattice and the

decrease of the crystallite size, among other factors, generates symmetry distortions which result in the broadening and/or the shift of the  $F_{2g}$  Raman signal [10]. A shift towards lower wavenumbers is expected when decreasing the crystallite size of ceria [11, 12], while the isomorphic substitution of the  $Ce^{4+}$  cations by other ones with lower ionic radii (as  $Fe^{3+}$ ) produces a shift towards higher wavenumbers [11, 12]. In our case, both contrary effects must be presented, and the observed red shift of the  $F_{2g}$  Raman band with the iron loading is indicative of the dominant role of the crystallite size effect. This conclusion agrees with that previously supported by Bao et al. [11].

The Fe-modified solids with low iron contents (5 and 10 atomic%) present a band around  $257\text{ cm}^{-1}$ . This band has not been previously discussed for Ce-Fe mixed systems, although similar ones have been described for Zr-doped  $CeO_2$  solids. Masui et al [36] observed a Raman band around  $307\text{ cm}^{-1}$  which they attributed to the formation of the tetragonal phase in the Zr-Ce mixed oxide. In a similar way, Fang et al [37] reported a band around  $297\text{ cm}^{-1}$  in Ce-Zr and Ce-Gd mixed oxide systems due to the tetragonal phase formation in the solid solution. Moreover, Liu et al. [38] described in the Raman spectra of Zr-modified  $CeO_2$  solids, not only the presence of a band around  $306\text{ cm}^{-1}$  but also its shifts to  $293\text{ cm}^{-1}$  when increasing the amount of Zr incorporated in the ceria. They established that the doping agent improves the generation of t phase-like lattice distortions resulting in the formation of a pseudocubic or tetragonal like ( $t''$ ) phase responsible of such Raman bands. A similar behavior could be considered in our system, where the introduction of low amounts of  $Fe^{3+}$  cations in the cubic network of ceria could result in a pseudocubic structure.

For the samples with high iron contents (CeFe25 and CeFe50 solids), two intense bands at  $206$  and  $264\text{ cm}^{-1}$  are detected (Figure 3). These bands along with the shoulders observed at around  $357\text{ cm}^{-1}$  and  $372\text{ cm}^{-1}$  suggest the existence of some kind of segregated iron oxides. The position and intensity ratio of such bands does not match those of pure  $Fe_2O_3$  (Figure 3, inset) suggesting its structural modification. Li et al. [27] have reported similar bands in the Raman spectra of a  $Ce_{0.7}Fe_{0.3}O_{2-\delta}$  solid, which they ascribed to  $Fe_2O_3$ . De Faria et al. in their Raman study of iron oxides and oxyhydroxides, observed changes in the relative intensity of Raman signals in natural and synthetic hematite due to changes in the crystallinity of the solids which generates changes in the sample orientation and in the band polarization behavior [35]. In our case, the observed modification in the relative intensity of the iron oxide bands could be due to the close interaction between cerium and iron oxides. Finally, since the existence of the Ce-Fe solid solution in the CeFe25 and CeFe50 solids is demonstrated by XRD (Figure 1), the presence of a distorted cubic structure as discussed above for the low Fe loaded mixed oxides cannot be fully discarded and, probably the characteristic Raman band (around  $257\text{ cm}^{-1}$ ) may overlap with those of the iron oxide.

Another interesting feature observed in the Raman spectra of the mixed oxides is the alteration of the relative intensity of the oxygen vacancies signal at  $598\text{ cm}^{-1}$  (Ov). This must be related with changes in the population of the oxygen vacancies in the material. In this sense, it is well established that the ratio between the areas of the Ov and  $F_{2g}$  Raman bands of ceria-based solids is characteristics of the concentration of the oxygen vacancies [7, 12, 39]. The obtained results are presented in Figure 4.

The Ov/ $F_{2g}$  area ratio increases when introducing 5 Fe atomic % in the ceria network, pass through a maximum for 10 atomic% iron contents and becomes almost zero for the



solid with 50 Fe atomic%. This behavior agrees with the work of Bao et al. that observed the maximum oxygen vacancies concentration in Ce-Fe mixed oxides prepared by precipitation with a 10 Fe atomic% [11]. The same authors observed the disappearance of the oxygen vacancies band for Fe atomic percentages of 40 and above, and conclude that doping with small amounts of Fe<sup>3+</sup> facilitates the formation of oxygen vacancies whereas large doping amounts annihilates them. This could be attributed to the existence of two different doping mechanisms to balance the charge when Ce<sup>4+</sup> is substituted by trivalent Fe<sup>3+</sup> cation, i) the vacancy compensation mechanism [39], that improves the generation of oxygen vacancies and ii) the dopant interstitial compensation mechanism, which eliminates them [11].

In a recent report, we have shown that, in a series Ce-Fe mixed oxides prepared by the propionate method [10], the oxygen vacancies of CeO<sub>2</sub> disappear after the doping with 10 atomic% of Fe. These results point out that not only the amount of iron but also the synthesis procedure controls the mechanism of formation of oxygen vacancies in the solid solution. In this sense, microemulsion is an adequate methodology to obtain homogeneous mixed materials where the isomorphic substitution of Ce by Fe is stabilized.

### 3.4. UV-Visible Spectroscopy

The UV-visible diffuse reflectance spectra of the prepared solids are presented in Figure 5. Pure CeO<sub>2</sub> shows absorption bands at 206, 237 and 270 nm due to the charge-transfer transition between O 2*p* and Ce 4*f* orbitals [40-42]. Pure Fe<sub>2</sub>O<sub>3</sub> presents several absorptions in the UV region (< 300 nm) due to O→Fe<sup>3+</sup> charge-transfer bands of isolated Fe ions in tetrahedral and octahedral coordination [43]. This transfer occurs from the highest lying O 2*p* orbitals to the half-occupied Fe 3*d* orbitals (*t*<sub>2*g*</sub>→*e*<sub>g</sub> *O<sub>h</sub>* symmetry and *e*→*t*<sub>2</sub> in *T<sub>d</sub>* symmetry) [41].

The spectrum of the bare iron oxide also shows a broad absorption band centered at 381 nm which has been previously assigned to oligomeric clusters of α-Fe<sub>2</sub>O<sub>3</sub> [41-43]. In the visible region (>450 nm), a main absorption around 533 nm, commonly associated to *d-d* (<sup>6</sup>A<sub>1g</sub>→<sup>4</sup>T<sub>1g</sub> and <sup>6</sup>A<sub>1g</sub>→<sup>4</sup>T<sub>1g</sub>) transitions in α-Fe<sub>2</sub>O<sub>3</sub> [41], is detected. Thus, as proposed from the XRD and Raman studies, our microemulsion prepared iron oxide has an α-Fe<sub>2</sub>O<sub>3</sub> (hematite) structure.

The spectra of the low loading mixed oxides resembles that of pure ceria, but a widening of the absorption edge and the appearance of absorption bands of α-Fe<sub>2</sub>O<sub>3</sub> is evident when increasing the iron content of the sample. The shift in the absorption edge is indicative of the Ce-Fe interaction. The calculated band gap of the solids considering direct transitions between the conduction and the valence bands with photon emissions [44, 45] are presented in Table 1.

The band gap value of our pure CeO<sub>2</sub> is similar to that reported in literature (3.2 eV) [45, 46]. The small difference with the reported value can be attributed to some morphology modifications [45]. The mixed oxides presented a progressive decrease in its band gap energy as the amount of doping metal increases. A similar observation has been reported for Ti, Mn, Fe and Co doped ceria solids by Yue et al. [46]. This effect has been explained because of the 3*d* transition metals supply unoccupied orbitals of lower energy than those of Ce 4*f*, decreasing that way the energy needed for the O 2*p* to unoccupied orbitals transition [42]. The band gap energy value is an evidence of the position and donating properties of the top of the valence band, and can be used as a

measure of the basicity of the solid [42]. Thus, the observed decrease in the band gap when increasing the iron content indicates the enhancement in the electronic properties (higher easiness of transport of electrons) in the CeO<sub>2</sub> structure by the presence of iron atoms.

In the visible region of the spectra, the broad adsorption at around 533 nm, characteristic of d-d transitions in  $\alpha$ -Fe<sub>2</sub>O<sub>3</sub>, is detected for the mixed solid with the highest iron content, CeFe50, confirming that way the slight segregation of this phase.

### 3.5. TPR

The TPR profile of the prepared solids is presented in Figure 6. For the pure CeO<sub>2</sub> two main signals can be detected. The first one at 486 °C, is attributed to the reduction of the surface shell and the high temperature signal at 764 °C to the reduction of the bulk of the material [13, 47, 48].

The TPR of bare Fe<sub>2</sub>O<sub>3</sub> sample presents three reduction peaks at 373, 590 and 724°C. The H<sub>2</sub> consumption of the peak at 373 °C corresponds to that required for the reduction of Fe<sub>2</sub>O<sub>3</sub> to Fe<sub>3</sub>O<sub>4</sub>, commonly reported as the first reduction step of the Fe<sub>2</sub>O<sub>3</sub> [49-51]. The broad reduction with maxima at 590 °C and 724 °C must be related with the reduction of Fe<sub>3</sub>O<sub>4</sub> to Fe<sup>0</sup>, which may follow different kinetics, as was discussed by Li et al. [50, 51], and probably through the formation of FeO as intermediate species, as proposed by Zhong et al. [52]. In the case of the mixed oxides, there are also several reduction peaks with a complex profile where the reduction of iron and cerium species overlaps. The peak at lower temperature, which for the CeFe5 sample appears at 397 °C, becomes more intense and shifts to lower temperatures with the load of iron in the material. This peak could be due to the first reduction step of Fe<sup>3+</sup> species [50, 51]. However, the simultaneous reduction, at least partially, of both surface Ce<sup>4+</sup> and Fe<sup>3+</sup> species have to be considered according with the reported behavior about the reduction of Zr, Zn and Fe doped CeO<sub>2</sub> [12, 48, 53]. The shift to lower temperatures demonstrates the synergy between these cations through the solid solution formation which generates mixed oxides with higher reducibility than pure CeO<sub>2</sub>.

The broad peaks at 627 °C and 598 °C for the CeFe10 and CeFe25 solids respectively, can be due to the intermediate reduction steps of Fe species to metallic Fe. Again, the reduction of part of the Ce<sup>4+</sup> cations in close contact with Fe ones could be also produced.

In the case of the CeFe50 solid, the only mixed oxide for which the solid solution formation and the segregation of  $\alpha$ -Fe<sub>2</sub>O<sub>3</sub> were suggested by the other characterization techniques, a new reduction peak at 434 °C is observed and the processes of high temperature appear as an only peak at 684 °C, This different profile of reduction must be related with the existence of different surface cerium and iron species (in the solid solution and/or in the segregated iron oxide) in intimate contact.

In order to establish a quantitative estimation of the reducibility of the considered solids, the reduction percentage (RP) of every system has been calculated according to equation 5.

$$RP = \frac{E_{HC}}{T_{HC}} \times 100 \quad (\text{Eq. 5})$$

where  $T_{HC}$  is the theoretical hydrogen consumption (in moles) needed for the complete reduction of all the reducible cations present in the amount of solid that was weighed for the TPR measurement, and  $E_{HC}$  is the experimental total hydrogen consumption measured during the TPR. For the calculation of  $T_{HC}$ , we have considered that all cations are initially in their maximum oxidation state. The results are presented in Table 1.

The pure oxides,  $CeO_2$  and  $Fe_2O_3$ , present the lowest and the highest reducibility percentage respectively. The mixed oxides exhibit an increase of their reducibility percentage until a maximum value ( $78 \pm 2\%$ ) for the high loaded solids ( $\geq 10$  Fe atomic%). This behavior suggests that the efficiency to reduce the reducible species is not significantly improved by the addition of more than 10 Fe atomic%, which agrees with the Raman results that found this iron content as the optimal value for the generation of the highest number of oxygen vacancies into the doped-ceria structure (Figure 4).

From all above, and according to the TPR analysis, we can conclude that the introduction of iron promotes the reducibility of the ceria structure, which is demonstrated by i) the increase in the reduction percentage of the solids up to 10 Fe atomic%, which could be related with the number of oxygen vacancies, and ii) by the lowering of the temperature at which the reduction processes takes place at the surface.

### 3.6. *Catalytic activity*

The catalytic performance of the prepared solids was evaluated in the oxidation of CO (TOX) and the preferential oxidation of CO in presence of  $H_2$  (PROX). The CO conversion during the CO oxidation is presented in Figure 7. The pure oxides exhibit lower catalytic activities than the mixed oxides, being the  $CeO_2$  the less active system.

The solid with the highest catalytic activity is the mixed oxide with the 10 Fe atomic%, which could be related at the first sight, with the highest number of oxygen vacancies in this solid (Figure 4). In this sense, this iron loading has been reported early as the optimal for achieving the major CO oxidation capability in Fe-modified ceria systems [10, 11]. In the work of Bao et al. [11] over Ce-Fe solids prepared by coprecipitation, this iron content also generates the major concentration in oxygen vacancies, in good agreement with our results over Ce-Fe mixed oxides prepared by microemulsion. However, in a recent paper we have presented a series of Ce-Fe mixed oxides obtained by the thermal decomposition of the respective metallic propionates where, although the most active material for CO oxidation is that of 10 Fe atomic%, the oxygen vacancies are not detected for this material. The conclusion of these works is that, without oxygen vacancies into the  $CeO_2$  framework, the iron species create structural sites with high electronic density which can act in a similar way than oxygen vacancies [10, 12].

In order to compare the catalytic activity showed by ceria modified solids with the same iron content but prepared by different methods, let us see the temperature for which the 50% CO conversion ( $T_{50}$ ) is achieved. In the case of a CeFe10 sample prepared by coprecipitation [11] this value is reported around 227 °C. However a similar sample prepared by the method of the thermal decomposition of propionates showed a  $T_{50}$  of 210 °C [10], that is very close to the value obtained in the present paper for the solid prepared by the microemulsion method. This suggests that those synthesis procedures

that improve the Ce-Fe interaction results in solids with improved catalytic properties towards CO oxidation.

Thus, not only the nature and concentration of the doping agent but also the homogeneity and the Ce-metal interaction of the mixed oxide, which depends on the synthesis method used, strongly determine the mechanism of formation of the oxygen vacancy (vacancy compensation [39] or elimination -dopant interstitial compensation-mechanisms [11]) and the catalytic activity in the CO oxidation reactions. In this sense, microemulsion method produces more homogeneous solids than those generated by other conventional methods, and is an attractive way of synthesizing materials with high potential applications as active catalytic supports.

On the other hand, although the CeFe50 solid does not present the Raman oxygen vacancies band (Figure 3), the Ce-Fe interaction allows considerable CO conversion levels (Figure 7), even higher than those of the CeFe25 solid, in spite of their similar reducibility percentage values (Table 1). The coexistence in the CeFe50 mixed oxide of the solid solution and the segregated  $\alpha$ -Fe<sub>2</sub>O<sub>3</sub> phase, may favor the catalytic properties of the material due to i) the rich electron sites created in the structure of the oxide by the presence of the Fe cations in the interstitial positions which can act as preferential sites of CO activation and ii) the presence of the perimeter of contact between the solid solution and the segregated metal oxide which could also be a favorable zone for the activation of the CO molecules, as recently proposed for a series of Zn-modified ceria oxides [6].

The catalytic activity presented as the CO conversion and the selectivity to CO oxidation of the prepared solids during the PROX reaction, is presented in Figure 8. As in the case of the TOX reaction, the pure oxides present lower CO conversions than mixed oxides, being the bare CeO<sub>2</sub> slightly more active than Fe<sub>2</sub>O<sub>3</sub>.

Again, the highest CO conversion is presented by the sample with the high amount of oxygen vacancies, the CeFe10 solid (Figure 8A). Besides this, the low loading systems have higher catalytic activities than those of high loadings. Since PROX reaction proceeds under reductant conditions and with a limited oxygen supply, the CO oxidation strongly depends on the oxygen release capacity of the solids. Then, the best catalytic properties of low loading samples could be due to the fact that those systems may stabilize more easily the formation of oxygen vacancies than those of high iron contents where the iron species in the interstitial positions can be slightly limiting the oxygen mobility into the oxide framework.

Nevertheless, the intrinsic CO oxidation ability of the Fe species along with the probable formation of active interfaces for the CO activation between the Fe<sub>2</sub>O<sub>3</sub> and the Ce-Fe solid solution surface, are responsible of the higher catalytic activity of the CeFe50 solid respect to the pure oxides.

In both CO oxidation reactions, the catalytic activity depends mainly on the oxygen activation and accessibility (from the atmosphere or from the structure). The Fe-doped ceria solids may release easily oxygen species from their structure and TPR studies demonstrate that the reducibility percentage increases at high iron contents. However, the results of the catalytic CO oxidation reactions (TOX and PROX) suggest that this improvement of the reducibility at high iron loadings is, probably, not reversible. The

solids with low amounts of iron incorporated must present a more reversible reducibility and, consequently, a superior oxygen exchange favoring the oxygen uptake/releasing process required for the CO oxidation.

All the Fe-doped solids present selectivities to CO oxidation close to 100% at temperatures below 120 °C (Figure 8B). However, in this range of temperatures, very low CO conversion is achieved (Figure 8A). Above 120 °C the selectivity decreases with the temperature. This result is in good agreement with previous works and is associated to the presence of the H<sub>2</sub> oxidation and the WGS or R-WGS reactions [12, 54], which are more evident at high temperatures. In a recent kinetic study performed on a Au/Ce-Fe catalyst [55], we established that the CO oxidation reaction present a lower specific activation energy (50 kJ/mol) than that of the H<sub>2</sub> oxidation (66.9 kJ/mol), being this fact the reason because the selectivity decreases when the temperature increases. On the other hand, the selectivity is slightly higher for the CeFe5 and CeFe10 solids than for the CeFe25, CeFe50 and pure CeO<sub>2</sub> ones, pointing out that the oxidation of CO is specially favored with respect to the H<sub>2</sub> oxidation for those catalysts loaded with low iron content. As demonstrated above, these materials present a more homogeneous modification of the cubic structure of the ceria network. This modification probably generates a kind of active sites more selective to the CO adsorption. In this sense, Scire et al. [56] observed the change of selectivity to CO oxidation in the PROX reaction on Au/Fe<sub>2</sub>O<sub>3</sub> catalysts depending on the chemical nature and oxidation state of gold and iron species in the surface of the materials. They concluded that the chemical nature of the active sites influences the CO/H<sub>2</sub> adsorbed molecules ratio in the surface coverage, promoting the observed changes in the overall selectivity of the process. Finally, despite of the low CO conversion in this material, the selectivity trend with temperature observed for pure Fe<sub>2</sub>O<sub>3</sub> is opposite to those described for the other solids above 160 °C, due to the absence of the Ce-Fe interaction.

#### **4. Conclusions**

A series of Fe-doped ceria solids with a good control of the chemical composition has been successfully achieved by the microemulsion method. For all the Fe metallic percentages evaluated (5, 10, 25 and 50 %) the formation of the solid solution was obtained, although the segregation of part of the iron species as  $\alpha$ -Fe<sub>2</sub>O<sub>3</sub> is detected for the mixed system with the highest iron content. As the amount of Fe incorporated into the CeO<sub>2</sub> matrix increases, the electronic transferring and the reducibility are enhanced.

The population of oxygen vacancies is maximum for the solid doped with 10 Fe atomic%. This behavior evidences that the microemulsion method allows obtaining homogeneous Ce-Fe mixed oxides where the isomorphic substitution of Ce<sup>4+</sup> cations by Fe<sup>3+</sup> ones takes place. This generates the formation of oxygen vacancies through an oxygen vacancies compensation mechanism even at high iron contents (25 atomic%). On the other hand, the CO oxidation performances are especially enhanced for the solids with low iron contents and high oxygen vacancies concentration. The optimal iron content (10 atomic%) represents the Ce/Fe atomic ratio where the maximum reversible oxygen exchange can be achieved. For the lowest iron content (5 atomic%) this reversible oxygen exchange is not enough improved and for the solids with 25 and 50 Fe atomic%, although they have a similar reducibility, this is not easily reversible, which is crucial for the activation of oxygen species required during the CO oxidation.

Thus, Ce-Fe systems prepared from microemulsion are very attractive to be considered as supports for depositing active phases capable of enhancing oxygen exchange ability of the whole system, allowing higher CO oxidation abilities.

## 5. Acknowledgments

Financial support for this work has been obtained from the Spanish Ministerio de Ciencia e Innovación (ENE2009-14522-C05-01) cofinanced by FEDER funds from the European Union, and from Junta de Andalucía (P09-TEP-5454). O.H. Laguna thanks the same Ministry for the FPI fellowship (BES-2007-14409) awarded, allowing a research stay at the Royal Institute of Technology (KTH) in Stockholm, Sweden.

## 6. References

- [1] M.I. Domínguez, F. Romero-Sarria, M.A. Centeno, J.A. Odriozola, *Applied Catalysis B: Environmental* 87 (2009) 245-251.
- [2] F. Romero-Sarria, A. Penkova, L.M. Martínez T, M.A. Centeno, K. Hadjiivanov, J.A. Odriozola, *Applied Catalysis B: Environmental* 84 (2008) 119-124.
- [3] T.V. Choudhary, D.W. Goodman, *Catalysis Today* 77 (2002) 65-78.
- [4] M.A. Centeno, M. Paulis, M. Montes, J.A. Odriozola, *Applied Catalysis A: General* 234 (2002) 65-78.
- [5] A. Martínez-Arias, M. Fernández-García, A.B. Hungría, A. Iglesias-Juez, O. Gálvez, J.A. Anderson, J.C. Conesa, J. Soria, G. Munuera, *Journal of Catalysis* 214 (2003) 261-272.
- [6] O.H. Laguna, M.A. Centeno, F. Romero-Sarria, J.A. Odriozola, *Catalysis Today* (2011) doi:10.1016/j.cattod.2011.1002.1015.
- [7] W.Y. Hernández, M.A. Centeno, F. Romero-Sarria, J.A. Odriozola, *Journal of Physical Chemistry C* 113 (2009) 5629-5635.
- [8] A. Martínez-Arias, M. Fernández-García, O. Gálvez, J.M. Coronado, J.A. Anderson, J.C. Conesa, J. Soria, G. Munuera, *Journal of Catalysis* 195 (2000) 207-216.
- [9] F.J. Pérez-Alonso, I. Melián-Cabrera, M. López Granados, F. Kapteijn, J.L.G. Fierro, *Journal of Catalysis* 239 (2006) 340-346.
- [10] O.H. Laguna, M.A. Centeno, G. Arzamendi, L.M. Gandía, F. Romero-Sarria, J.A. Odriozola, *Catalysis Today* 157 (2010) 155-159.
- [11] H. Bao, X. Chen, J. Fang, Z. Jiang, W. Huang, *Catalysis Letters* 125 (2008) 160-167.
- [12] O.H. Laguna, F. Romero Sarria, M.A. Centeno, J.A. Odriozola, *Journal of Catalysis* 276 (2010) 360-370.
- [13] W.Y. Hernández, F. Romero-Sarria, M.A. Centeno, J.A. Odriozola, *Journal of Physical Chemistry C* 114 (2010) 10857-10865.
- [14] F.J. Pérez-Alonso, M. López Granados, M. Ojeda, P. Terreros, S. Rojas, T. Herranz, J.L.G. Fierro, M. Gracia, J.R. Gancedo, *Chemistry of Materials* 17 (2005) 2329-2339.
- [15] F.J. Pérez-Alonso, T. Herranz, S. Rojas, M. Ojeda, M. López Granados, P. Terreros, J.L.G. Fierro, M. Gracia, J.R. Gancedo, *Green Chemistry* 9 (2007) 663-670.
- [16] F.J. Pérez-Alonso, M.L. Granados, M. Ojeda, T. Herranz, S. Rojas, P. Terreros, J.L.G. Fierro, M. Gracia, J.R. Gancedo, *Journal of Physical Chemistry B* 110 (2006) 23870-23880.
- [17] M. Boutonnet, S. Lögdberg, E. Elm Svensson, *Current Opinion in Colloid & Interface Science* 13 (2008) 270-286.

- [18] M. Sanchez-Dominguez, L.F. Liotta, G. Di Carlo, G. Pantaleo, A.M. Venezia, C. Solans, M. Boutonnet, *Catalysis Today* 158 (2010) 35-43.
- [19] S. Eriksson, U. Nylén, S. Rojas, M. Boutonnet, *Applied Catalysis A: General* 265 (2004) 207-219.
- [20] B.J. Palla, D.O. Shah, P. Garcia-Casillas, J. Matutes-Aquino, *Journal of Nanoparticle Research* 1 (1999) 215-221.
- [21] S. Nassos, E. Elm Svensson, M. Boutonnet, S.G. Järås, *Applied Catalysis B: Environmental* 74 (2007) 92-102.
- [22] S. Nassos, E.E. Svensson, M. Nilsson, M. Boutonnet, S. Järås, *Applied Catalysis B: Environmental* 64 (2006) 96-102.
- [23] E.E. Svensson, S. Nassos, M. Boutonnet, S.G. Järås, *Catalysis Today* 117 (2006) 484-490.
- [24] G. Leofanti, M. Padovan, G. Tozzola, B. Venturelli, *Catalysis Today* 41 (1998) 207-219.
- [25] A.R. West, *Solid State Chemistry and its Applications*, New York, 1990.
- [26] Z. Tianshu, P. Hing, H. Huang, J. Kilner, *Journal of Materials Processing Technology* 113 (2001) 463-468.
- [27] K. Li, H. Wang, Y. Wei, D. Yan, *Applied Catalysis B: Environmental* 97 (2010) 361-372.
- [28] F. Romero-Sarria, J.C. Vargas, A.-C. Roger, A. Kiennemann, *Catalysis Today* 133-135 (2008) 149-153.
- [29] S. Rossignol, C. Micheaud-Especel, D. Duprez, F.V.M.S.M. Avelino Corma, G.F. José Luis, *Studies in Surface Science and Catalysis*, Elsevier, 2000, pp. 3327-3332.
- [30] J.E. Spanier, R.D. Robinson, F. Zhang, S.W. Chan, I.P. Herman, *Physical Review B - Condensed Matter and Materials Physics* 64 (2001) 2454071-2454078.
- [31] C. Baratto, P.P. Lottici, D. Bersani, G. Antonioli, G. Gnappi, A. Montenero, *Journal of Sol-Gel Science and Technology* 13 (1999) 667-671.
- [32] T.P. Martin, R. Merlin, D.R. Huffman, M. Cardona, *Solid State Communications* 22 (1977) 565-567.
- [33] K.F. McCarty, *Solid State Communications* 68 (1988) 799-802.
- [34] S.H. Shim, T.S. Duffy, *American Mineralogist* 87 (2002) 318-326.
- [35] D.L.A. De Faria, S. Venâncio Silva, M.T. De Oliveira, *Journal of Raman Spectroscopy* 28 (1997) 873-878.
- [36] T. Masui, Y. Peng, K.-i. Machida, G.-y. Adachi, *Chemistry of Materials* 10 (1998) 4005-4009.
- [37] P. Fang, M.-F. Luo, J.-Q. Lu, S.-Q. Cen, X.-Y. Yan, X.-X. Wang, *Thermochimica Acta* 478 (2008) 45-50.
- [38] L. Liu, Z. Yao, B. Liu, L. Dong, *Journal of Catalysis* 275 (2010) 45-60.
- [39] A. Trovarelli, *Comments on Inorganic Chemistry* 20 (1999) 263-284.
- [40] S. Tsunekawa, T. Fukuda, A. Kasuya, *Journal of Applied Physics* 87 (2000) 1318-1321.
- [41] A.S. Reddy, C.-Y. Chen, C.-C. Chen, S.-H. Chien, C.-J. Lin, K.-H. Lin, C.-L. Chen, S.-C. Chang, *Journal of Molecular Catalysis A: Chemical* 318 (2010) 60-67.
- [42] M.Á. Centeno, C. Portales, I. Carrizosa, J.A. Odriozola, *Catalysis Letters* 102 (2005) 289-297.
- [43] M. Schwidder, M.S. Kumar, K. Klementiev, M.M. Pohl, A. Brückner, W. Grünert, *Journal of Catalysis* 231 (2005) 314-330.
- [44] P.C.A. Brito, D.A.A. Santos, J.G.S. Duque, M.A. Macêdo, *Physica B: Condensed Matter* 405 (2010) 1821-1825.

- [45] C. Ho, J.C. Yu, T. Kwong, A.C. Mak, S. Lai, *Chemistry of Materials* 17 (2005) 4514-4522.
- [46] L. Yue, X.M. Zhang, *Journal of Alloys and Compounds* 475 (2009) 702-705.
- [47] L. Ilieva, G. Pantaleo, I. Ivanov, R. Zanella, A.M. Venezia, D. Andreeva, *International Journal of Hydrogen Energy* 34 (2009) 6505-6515.
- [48] S. Damyanova, B. Pawelec, K. Arishtirova, M.V.M. Huerta, J.L.G. Fierro, *Applied Catalysis A: General* 337 (2008) 86-96.
- [49] R. Brown, M.E. Cooper, D.A. Whan, *Applied Catalysis* 3 (1982) 177-186.
- [50] S. Li, S. Krishnamoorthy, A. Li, G.D. Meitzner, E. Iglesia, *Journal of Catalysis* 206 (2002) 202-217.
- [51] S. Li, A. Li, S. Krishnamoorthy, E. Iglesia, *Catalysis Letters* 77 (2001) 197-205.
- [52] Z. Zhong, J. Highfield, M. Lin, J. Teo, Y.-f. Han, *Langmuir* 24 (2008) 8576-8582.
- [53] S. Ricote, G. Jacobs, M. Milling, Y. Ji, P.M. Patterson, B.H. Davis, *Applied Catalysis A: General* 303 (2006) 35-47.
- [54] G.W. Roberts, P. Chin, X. Sun, J.J. Spivey, *Applied Catalysis B: Environmental* 46 (2003) 601-611.
- [55] G. Arzamendi, I. Uriz, P.M. Diéguez, O.H. Laguna, W.Y. Hernández, A. Álvarez, M.A. Centeno, J.A. Odriozola, M. Montes, L.M. Gandía, *Chemical Engineering Journal* 167 (2011) 588-596.
- [56] S. Scirè, C. Crisafulli, S. Minicò, G.G. Condorelli, A. Di Mauro, *Journal of Molecular Catalysis A: Chemical* 284 (2008) 24-32.



**TABLE**

Table 1. Chemical composition and other physical-chemical properties of the prepared solids (after calcination at 500 °C for 2 h)

|                                | Ce<br>Atomic % | Fe<br>Atomic % | BET area<br>(m <sup>2</sup> /g) | Pore volume<br>(cm <sup>3</sup> /g) | Crystallite size*<br>(Å) | Band gap<br>(eV) | Reducibility<br>percentage<br>(%) |
|--------------------------------|----------------|----------------|---------------------------------|-------------------------------------|--------------------------|------------------|-----------------------------------|
| CeO <sub>2</sub>               | 100            | 0              | 66                              | 0.1470                              | 97                       | **               | 48                                |
| CeFe5                          | 94.2           | 5.8            | 97                              | 0.2362                              | 90                       | 3.09             | 65                                |
| CeFe10                         | 89.2           | 10.8           | 81                              | 0.2835                              | 87                       | 2.45             | 76                                |
| CeFe25                         | 73.4           | 26.6           | 84                              | 0.2988                              | 79                       | 2.34             | 80                                |
| CeFe50                         | 45.6           | 54.4           | 110                             | 0.3486                              | 62                       | 1.96             | 78                                |
| Fe <sub>2</sub> O <sub>3</sub> | 0              | 100            | 33                              | 0.1850                              | 139                      | 1.53             | 93                                |

\*Calculated with the Scherrer equation

\*\* Not calculated

## FIGURE CAPTIONS

Figure 1. XRD patterns of the prepared solids: (A) General XRD patterns; (B) Enlarged view of the reflection (200) in the XRD profiles of the Fe-doped solids

Figure 2. Modification of the cell parameter with the iron content of the mixed oxides

Figure 3. Raman spectra of the prepared solids

Figure 4.  $O_v/F_{2g}$  area ratio for the pure and Fe-doped ceria

Figure 5. UV-Visible spectroscopy of the prepared solids

Figure 6. TPR profile of the prepared solids

Figure 7. CO conversion during the TOX reaction of the prepared solids

Figure 8. Catalytic activity during the PROX reaction of the prepared solids: (A) CO conversion; (B) Selectivity to CO conversion

# FIGURES

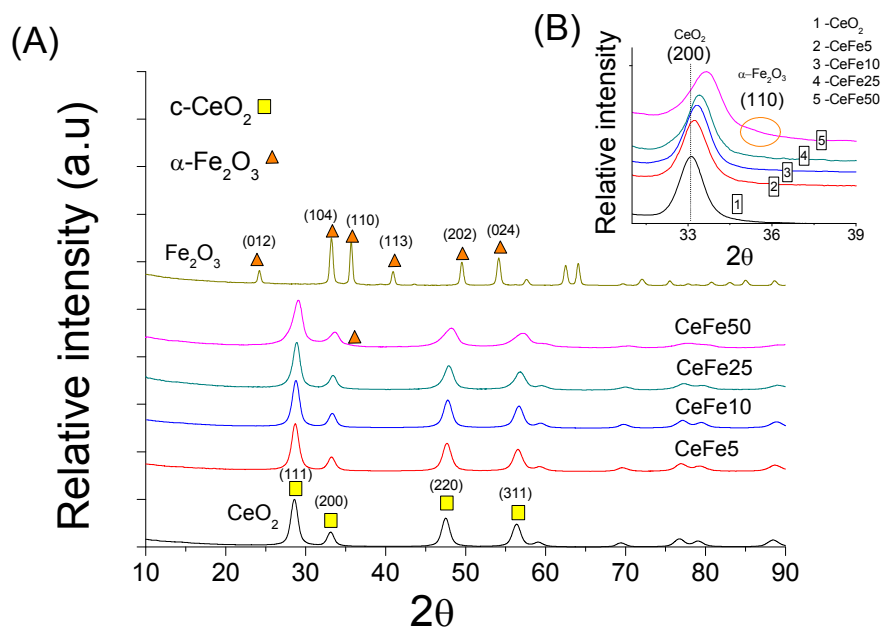
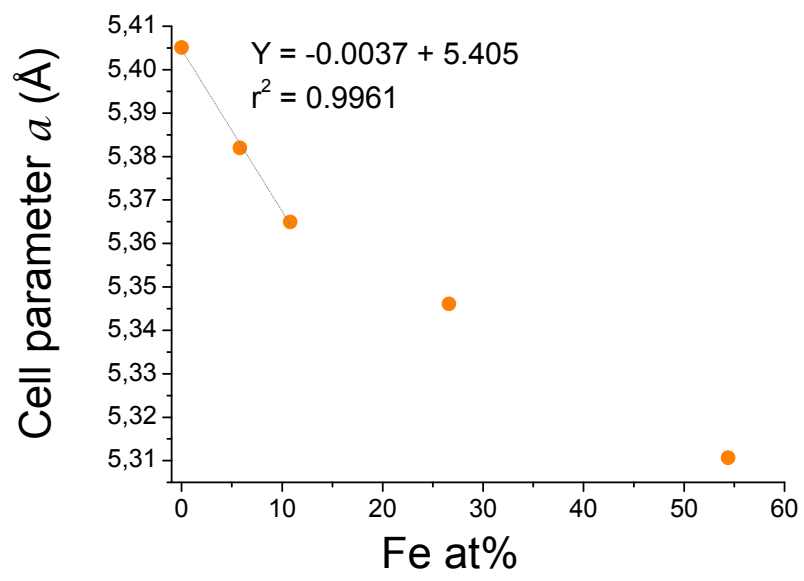
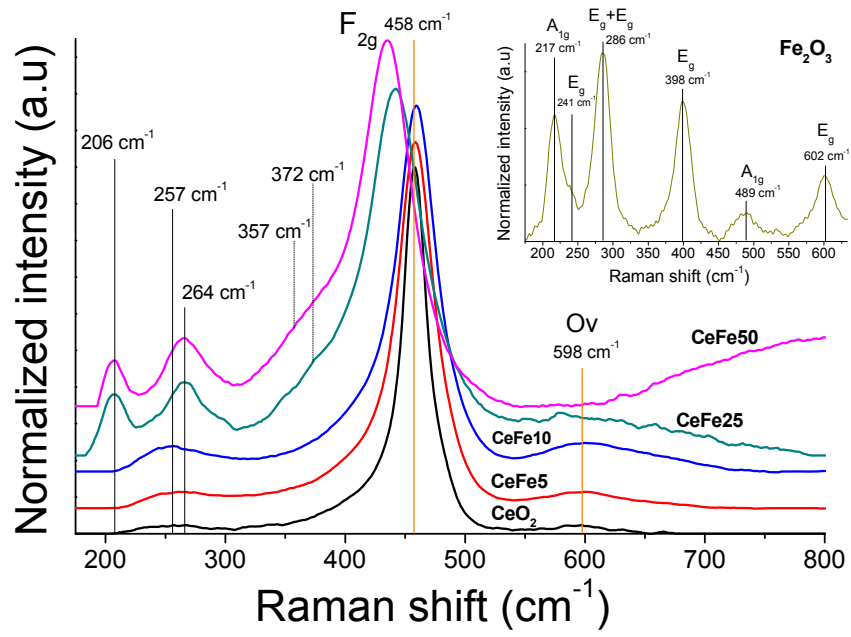


Figure 1



**Figure 2**



**Figure 3**

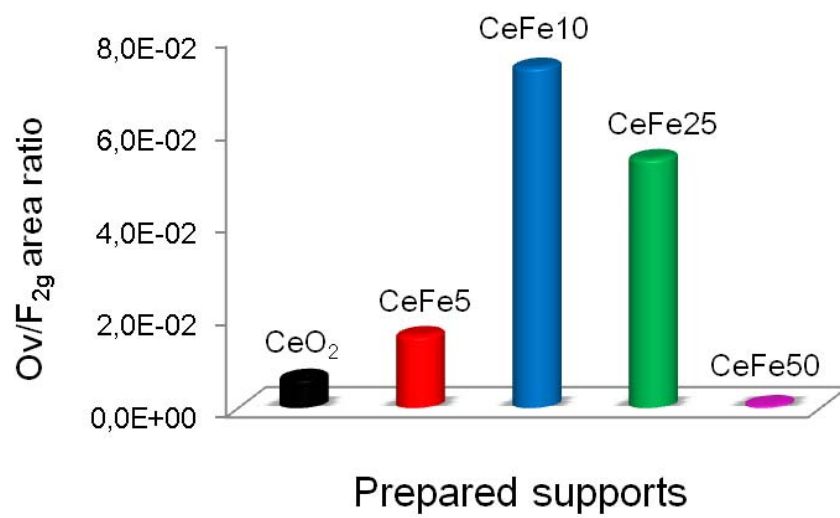


**Figure 4**

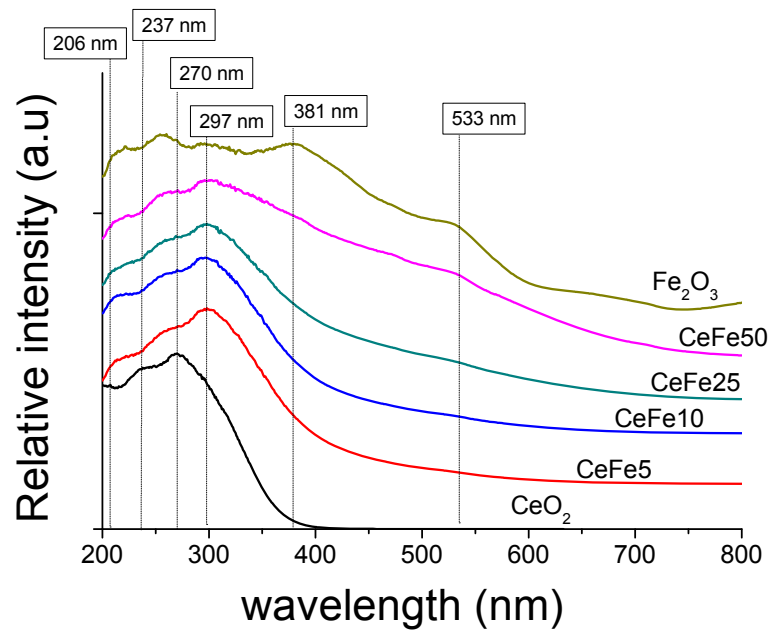


**Figure 5**

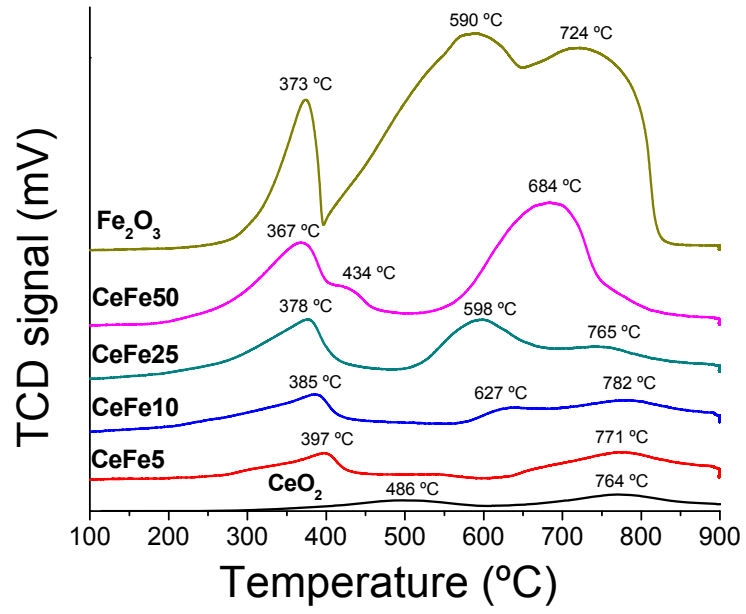


**Figure 6**



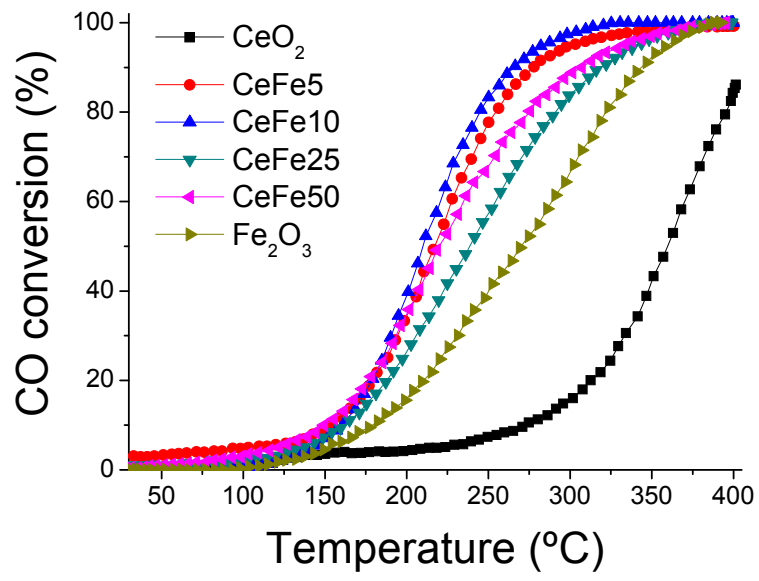
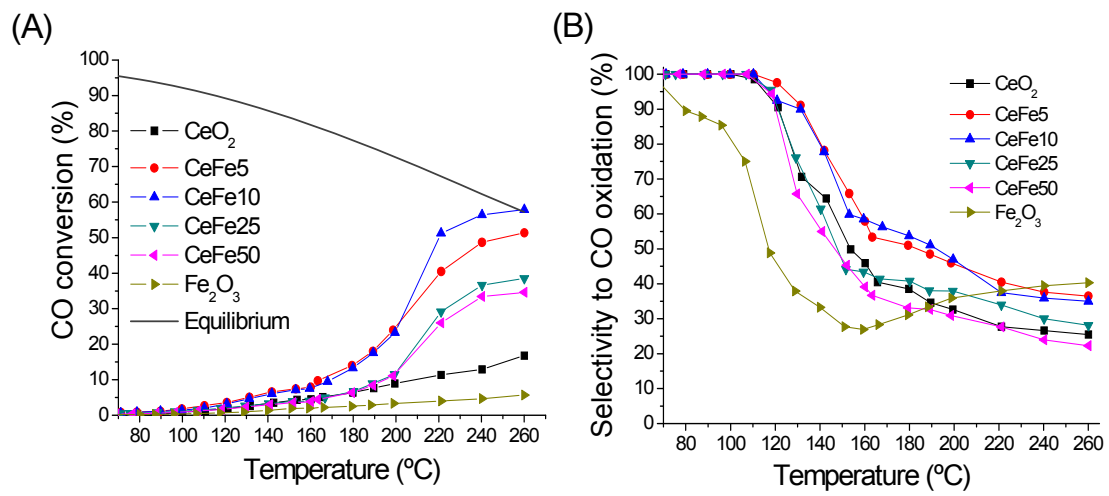


Figure 7



**Figure 8**